



Research paper

Bifunctional Co- and Ni- ferrites for catalyst-assisted chemical looping with alcohols



N.V.R. Aditya Dharanipragada^a, Vladimir V. Galvita^{a,*}, Hilde Poelman^a, Lukas C. Buelens^a, Christophe Detavernier^b, Guy B. Marin^a

^a Laboratory for Chemical Technology, Ghent University, Technologiepark 914, B-9052, Ghent, Belgium

^b Department of Solid State Sciences, Ghent University, Krijgslaan 281, S1, B-9000, Ghent, Belgium

ARTICLE INFO

Keywords:

Catalyst-assisted chemical looping
Oxygen storage material
CO₂ utilization
Bifunctional material

ABSTRACT

Ferrite materials were applied for catalyst-assisted chemical looping with two different alcohol fuels, methanol and an ethanol-water mixture (1:1 mol ratio), at 550 °C and 750 °C respectively. CO₂ was used for reoxidation, resulting in the production of CO. The structural characteristics, CO formation and stability of a range of x CoFe₂O₄/NiFe₂O₄ (x = 20 – 100 wt%) modified with CeZrO₂ were investigated through STEM and in situ XRD. Crystallographic changes during two consecutive H₂-TPR and CO₂-TPO cycles were followed using in situ XRD. Further, the long term stability was assessed during one hundred isothermal chemical looping redox cycles using H₂ for reduction and CO₂ for reoxidation. The 20 wt% CoFe₂O₄ material could be reduced and reoxidized to the as prepared state without loss in oxygen storage capacity. In 80 wt% CoFe₂O₄ however, deactivation due to phase segregation into Co and Fe₃O₄ along with material sintering occurred. On the other hand, all NiFe₂O₄ materials modified with CeZrO₂ suffered from sintering as well as phase segregation into separate Ni and Fe₃O₄ phases, which could not be restored into the original spinel (NiFe₂O₄) phase. During chemical looping with methanol, carbon formation was observed on CoFe₂O₄/NiFe₂O₄ ferrites modified with CeZrO₂. 20 wt% CoFe₂O₄ was the best performing material with a CO yield of ~40 mol CO kg_{CoFe₂O₄}⁻¹, i.e. almost twice the theoretical amount. This high CO yield was ascribed to the oxidation of carbon formed upon material reduction. During chemical looping with the ethanol-water mixture however, the CO yield remained low (~13 mol CO kg_{CoFe₂O₄}⁻¹) because of incomplete conversion of CH₄ and water. A pre-catalyst bed configuration for complete conversion of CH₄ and water is proposed.

1. Introduction

Since the industrial revolution, human dependence on fossil fuels has increased exponentially. This has resulted in increased emission of greenhouse gases like CO₂ and CH₄, which contribute to global warming [1,2]. Hence, there is a need to minimize our dependence on fossil fuels and to shift towards more clean energy sources [3,4]. The potential technologies which can achieve this reduction in greenhouse gas emission by minimizing the consumption of fossil fuels are fuel cell driven processes. Fuel cells are the most efficient way of directly converting chemical energy to electrical energy. The most common fuel cells are based on proton conducting electrolytes (PEMFC: proton-exchange membrane fuel cell), which require high purity hydrogen as fuel. Solid oxide fuel cells (SOFCs) on the other hand are fuel flexible and can oxidize essentially any fuel containing a mixture of hydrocarbons and even carbon, because the electrolyte transports an oxygen

ion. SOFCs capability of achieving high power densities is based on oxygen-ion conductors that operate at high temperature. Over the past decade, considerable progress has been achieved in bringing down the working temperature to an intermediate range between 350 °C–700 °C [5–7] and in reaching high stability of the anode under fuels other than hydrogen [8–10]. It has been established that even CO can be used as a fuel in SOFCs [8,11–14].

The latter can be generated from renewable fuels (biogas and bioethanol) and carbon dioxide through dry reforming. An attractive alternative process which can produce CO from CO₂ for SOFC technologies is chemical looping [15–17]. This is a two-step cyclic process where in the first step, an oxygen storage material is reduced by fuel (Fig. 1). In the second step, CO₂ is used for reoxidation to regenerate the material resulting in production of CO, which can serve as fuel for the SOFC. Iron oxides are the most widely preferred oxygen carriers in chemical looping CO₂ utilization, due to their redox activity with CO₂,

* Corresponding author.

E-mail address: Vladimir.Galvita@UGent.be (V.V. Galvita).

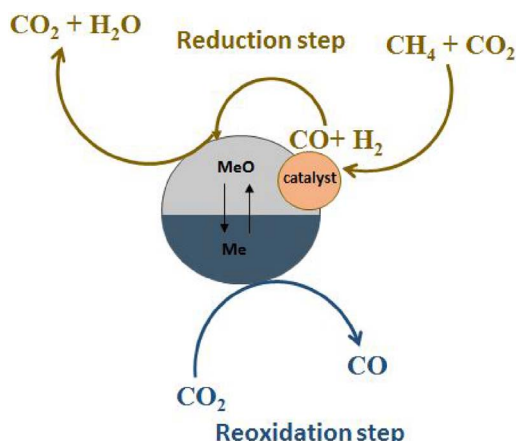


Fig. 1. Catalyst-assisted chemical looping using a bifunctional material.

high oxygen storage capacity, abundant availability and environmentally friendly nature [18–22]. When natural hydrocarbon containing feeds (e.g. biogas, $\text{CH}_4 + \text{CO}_2$) are employed for reduction, the overall production of CO is determined by the kinetics of the slower step, i.e. the reduction of iron oxide with CH_4 [23–26]. The presence of CO_2 in the feed and product stream slows down the reduction rate. In order to improve the kinetics of this step, an extra catalyst component (e.g. Ni, Co) can be added to the oxygen storage material to first convert CH_4 [24,27,28].

Addition of such a catalyst component to the iron oxide assists in CH_4 conversion to CO and H_2 through catalytic dry reforming. Subsequently, this mixture of CO + H_2 reduces the iron oxide oxygen storage material, producing CO_2 and H_2O (Fig. 1). The material thus acts both as an oxygen carrier and as a catalyst, hence it is termed bifunctional material and the process is called catalyst-assisted chemical looping [24,29].

In view of designing materials with both catalytic and oxygen storage properties, ferrites can be of interest as they offer both these properties. They have Co or Ni as a catalyst component and an oxygen storage component in the form of Fe. Moreover, ferrites are widely used as bifunctional materials due to their high oxygen storage capacity, easy reducibility (350 °C–550 °C) [30,31]. To improve the stability of the Co- and Ni-ferrites, which tend to deactivate rapidly, promoter elements can be added. Among the promoter candidates, CeZrO_2 stands out as it shows high stability along with redox activity in a CO_2 environment and also possesses desired mechanical properties [32].

As for chemical looping fuel, feedstocks containing alcohols, especially methanol and ethanol, are promising towards clean energy production due to their high hydrogen to carbon ratio, easy biomass derivability, high energy density as liquid fuel and easy storage [33–35]. Both methanol and ethanol have been applied as fuel in chemical looping over ferrite materials towards high purity hydrogen production [30,31,36–38].

In the present study, the applicability of CeZrO_2 modified Ni- and Co-ferrites in catalyst assisted chemical looping with ethanol, ethanol-water and methanol for CO_2 conversion to CO has been investigated. In the first step, methanol or ethanol are used as reducing agents. Methanol decomposes into CO and H_2 , whereas ethanol decomposes into CH_4 in addition to CO and H_2 . The decomposition reactions are enabled by the catalyst component. The mixtures of CO + H_2 or $\text{CH}_4 + \text{CO} + \text{H}_2$ reduce the oxygen storage component, thereby being converted to CO_2 and H_2O . The amount of CO that is produced in the second step of chemical looping, depends on the oxygen storage capacity and the degree of reduction that can be achieved in the first step. Therefore, this investigation is focused on the assessment of material stability and activity of CeZrO_2 promoted ferrite materials towards catalyst assisted chemical looping processes.

2. Experimental procedures

2.1. Material preparation

Ferrite materials with varying loadings ($x\text{CoFe}_2\text{O}_4/\text{NiFe}_2\text{O}_4 - \text{CeZrO}_2$, $x = 20, 50, 80$ and 100 wt%) were synthesized by means of co-precipitation. The following precursors were used: $\text{Fe}(\text{NO}_3)_3 \cdot 9\text{H}_2\text{O}$ (99.99 + %, Sigma-Aldrich[®]), $\text{Co}(\text{NO}_3)_2 \cdot 6\text{H}_2\text{O}$ (99.99%, Sigma-Aldrich[®]), $\text{Ni}(\text{NO}_3)_2 \cdot 6\text{H}_2\text{O}$ (99.99%, Sigma-Aldrich[®]), $\text{Ce}(\text{NO}_3)_3 \cdot 6\text{H}_2\text{O}$ (99.99%, Sigma-Aldrich[®]) and $\text{ZrO}(\text{NO}_3)_2 \cdot x\text{H}_2\text{O}$ (99.99%, Sigma-Aldrich[®]). The pH was controlled by dropwise addition of NH_4OH under stirring. The precipitate obtained was recovered and dried in an oven at 120 °C for 12 h. All materials were then calcined at 650 °C for 6 h and at 750 °C for the chemical looping process with ethanol. The ferrite materials modified with CeZrO_2 are represented as $x\text{wt\% CoFe}_2\text{O}_4/\text{NiFe}_2\text{O}_4$, where x represents the ferrite loading.

2.2. Characterization: x-Ray diffraction (XRD), scanning transmission electron microscopy (STEM) and Brunauer–Emmett–Teller (BET)

The crystalline phases were determined using a Siemens Diffractometer Kristalloflex D5000, with $\text{Cu K}\alpha$ ($\lambda = 0.154$ nm) radiation. The XRD patterns were collected in a 2θ range from 10° to 80° with a step of 0.04°. The crystallite size was calculated using the Scherrer equation by fitting a Gaussian function to the four most intense characteristic peaks to obtain the peak width at half maximum.

Morphological and local elemental analysis were performed using a JEOL JEM-2200FS: Cs-corrected, operated at 200 kV, equipped with a Schottky-type field-emission gun (FEG), EDX JEOL JED-2300D and JEOL in-column omega filter (EELS). Specimens were prepared by immersion of a lacey carbon film on copper support grid and particles sticking to the grid were investigated. Elemental mapping was performed by EDX. A beryllium specimen retainer was used to remove secondary X-ray fluorescence.

The Brunauer–Emmet–Teller (BET) surface area was determined by N_2 adsorption (five point BET method) using a Micromeritics Gemini 2360. Before carrying out the experiment, samples were outgassed for 3 h at 200 °C in order to remove the adsorbates.

2.3. Redox properties

The redox properties of the ferrite materials were investigated using in situ XRD and conventional TPR-TPO techniques. The phase changes during the redox processes were identified using in situ XRD and the bulk consumption was monitored using conventional TPR-TPO. Finally, the phase transformations were correlated to bulk consumption. The total amount of available oxygen is tabulated below.

2.3.1. In situ X-Ray diffraction (XRD) analysis

The crystallographic transformations during H_2 -TPR and CO_2 -TPO were followed by in situ XRD (Bruker-AXS D8 Discover) with $\text{Cu K}\alpha$ radiation source ($\lambda = 0.154$ nm). The setup consisted of a homebuilt reaction chamber with a Kapton foil window for X-ray transmission and a linear Vantec detector covering 20° with an angular resolution of 0.1° in 2θ. Approximately 10 mg of powder was spread on a single crystal Si wafer. No interaction between the Si wafer and sample was observed. Prior to the start of experiment, the chamber was pumped down to a base pressure of 5 Pa and purged with helium. 10 mol% H_2/He and pure CO_2 were employed for reduction and oxidation treatment. All gas flows were maintained at 30 Nml/s.

A uniform ramp rate of 20 °C/min up to a temperature of 700 °C was used during H_2 -TPR and CO_2 -TPO. Full XRD scans (10° to 65° with a step of 0.1°) were performed after each H_2 -TPR and CO_2 -TPO at room temperature under helium flow. The materials were subjected to repeated redox treatments, with two cycles of H_2 -TPR and CO_2 -TPO to study the phase transformations during these treatments.

2.3.2. Conventional TPR-TPO analysis

The redox properties were investigated during two consecutive cycles of H₂-TPR and CO₂-TPO in a U-shape quartz reactor containing a K-type thermocouple to measure temperature (Micromeritics Autochem II 2920). Approximately 30 mg of material was loaded in the reactor and ramped from room temperature up to 700 °C at a constant rate of 20 °C/min. The outlet gas compositions were monitored using a TCD detector and all the gas flows were maintained at 1.2 Nml/s (0.05 mmol/s).

2.4. Stability (H₂/CO₂ and alcohol/CO₂)

The isothermal redox stability (H₂/CO₂) and catalyst-assisted chemical looping experiments (methanol/CO₂, ethanol/CO₂, and ethanol-water mixture/CO₂) were carried out at atmospheric pressure in a quartz tube reactor (i.d. 10 mm). Approximately 100 mg of material was packed between quartz wool plugs. The temperature of the sample bed was monitored using K-type thermocouples and experiments were carried out at two different temperatures, depending on the reducing agent.

Redox stability experiments were performed at 550 °C for one hundred chemical looping cycles using H₂ (10 mol% H₂/He) as reducer and CO₂ (100 mol%) as oxidizer. The chemical looping experiments with methanol were also performed at the same temperature (550 °C) using methanol as reducing gas (10 mol% CH₃OH/He) and CO₂ (100 mol%) for reoxidation. The chemical looping experiments with ethanol were carried out at 750 °C with pure ethanol, as well as using a mixture of ethanol and water (1:1 mol ratio). 10 mol% of this mixture in He was introduced during the reduction step and CO₂ (100 mol%) was used for reoxidation. The total flow rate of gases into the reactor was kept constant at 5 Nml/s (0.2 mmol/s) for reducing, oxidizing and purge gases by means of Brooks mass flow controllers. The amounts of methanol and ethanol during the reduction half cycles were 10 times higher than the amount of available oxygen to ensure complete reduction of the materials.

The as prepared bifunctional materials were subjected to fifteen chemical looping cycles using ethanol and methanol. Each chemical looping experiment cycle consisted of a pulse with reducing gas followed by an oxidizing gas (CO₂) with He purge in between. The gases were pulsed for a time period of 180 s in each of these experiments.

In addition to the stability experiments, a study on CO yield was performed by varying the reduction times using methanol and ethanol from 60 to 180, 300 and 480 s. In the oxidation half cycle, CO₂ was used for material reoxidation. All the gas flow rates were 5 Nml/s (0.2 mmol/s).

The consumption of reducing and oxidizing gases during the process was monitored online using an OmniStar Pfeiffer mass spectrometer (MS), whose response was systematically calibrated with reference gases. A carbon balance with a maximum deviation of 15% was obtained and He was used as an internal standard.

The CO yield calculation is given by Eq. (1):

$$Y_{CO} = \frac{n_{CO}}{W_s} \quad (1)$$

Y_{CO} = Yield of CO produced in the reoxidation half cycle (mol kg⁻¹ ferrite);

n_{CO} = Mole of CO produced in the reoxidation half cycle (mol);

W_s = Mass of ferrite in the reactor (kg);

The theoretical CO yields from the Co- and Ni-ferrites were calculated according to the following equations:



Under the assumption that the ferrite phase is restored in both the materials during reoxidation by CO₂, the theoretical CO yield was

calculated (Eq. (2) & (3)) to be ~17 mol CO kg⁻¹ ferrite.

In order to compare the results with steady-state processes, multiple parallel reactor operation was examined for a continuous production of CO. The CO space time yield for a multi-tubular reactor concept was calculated by a dynamic simulation during redox cycles based on chemical looping operation in a single reactor. Such a multi-tubular reactor configuration is similar to a multi-column configuration in a pressure-swing adsorption process, where each column is cycled between adsorption and regeneration, allowing continuous processing of a given feed stream. The space time yield was determined based on the concept that all single reactors are operated in chemical looping regime, but one after the other, i.e. with a delay relative to the previous one [22,39]. Thus, by switching the feed flows of reducing and reoxidizing gases at discrete time intervals (Supplementary information Fig. S1), there is continuous operation of each reactor, eventually generating a permanent periodic regime. The time delay and the number of reactors in operation are based on the experimental results obtained for a single reactor. The space time yield (STY_M) for such a configuration is then simulated by summing the contributions of all single reactors and subsequent division by the number of operating reactors in oxidation mode (Eq. (4)). A time delay of 45 s with 4 reactors (N_{ox}) operating in parallel was used.

$$STY_M = \frac{\sum F_{CO}}{N_{ox} W_s} = \frac{\sum STY}{N_{ox}} \quad (4)$$

STY_M = Spacetimeyieldfromthemulti

– tubularreactorconfiguration(mol kg⁻¹ ferrite s⁻¹);

STY = SpacetimeyieldofCO(mol kg⁻¹ ferrite s⁻¹);

F_{CO} = OutletmolarflowrateofCO(mol CO s⁻¹);

W_s = Mass of ferrite in a single reactor (kg);

N_{ox} = Number of reactors in oxidation mode (-).

The conversion of alcohol when using methanol as reducing feed remained ~100% throughout the redox cycles at 550 °C in both the ferrites. When using ethanol as reducing feed at 750 °C, complete conversion is never achieved, the conversion values for 20wt%CeZrO₂-CoFe₂O₄ and 20wt%CeZrO₂-NiFe₂O₄ varied between 95% and 87% respectively.

2.5. Phase diagram

The EkviCalc software package [40] was used for thermodynamic property calculations for solid and gas phase species. The thermochemical calculations are carried out at specific temperature and pressure by assuming a closed system with an initial amount of selected reactant species. The equilibrium criterion is the minimization of the Gibbs free energy G_{p,T} (Eq. (5)) of the system at these specified conditions:

$$dG_{p,T} = \sum_{i=1}^m \mu_i dn_i = 0 \quad (5)$$

In Eq. (5), m (–) is the number of reactant and product species, μ_i (J/mol) is the chemical potential of species i at pressure p (bar) and temperature T (K), n_i (mol) is the amount of species i and G_{p,T} (J) is the Gibbs free energy of the system at pressure p and temperature T.

In the present investigation, thermodynamic calculations were performed concerning pure ferrites (NiFe₂O₄/CoFe₂O₄) in gas mixtures of CO + CO₂ and H₂ + H₂O by varying the mole fraction of CO and H₂ between 0 and 1 in the respective mixtures. The most stable metal oxide phase was then determined as a function of the gas phase composition and temperature, resulting in a phase diagram for the ferrite materials

Table 1
The theoretical oxygen storage capacity of ferrite materials.

Sample	O in $\text{CoFe}_2\text{O}_4/\text{NiFe}_2\text{O}_4$ (mol/kg)	O in CeZrO_2 (mol/ kg)	Total (mol/ kg)
20wt% CoFe_2O_4	0.3418	0.1520	0.4939
50wt% CoFe_2O_4	0.8547	0.0950	0.9497
80wt% CoFe_2O_4	1.3675	0.0380	1.4055
20wt% NiFe_2O_4	0.3418	0.1520	0.4939
50wt% NiFe_2O_4	0.8547	0.0950	0.9497
80wt% NiFe_2O_4	1.3675	0.0380	1.4055

(Table 1).

3. Results and discussion

3.1. Material characterization

3.1.1. XRD and BET

The as prepared materials were characterized using powder XRD to determine their crystalline phases. The diffraction patterns of pure CoFe_2O_4 and Co-ferrites modified with CeZrO_2 are shown in Fig. 2a. Bulk CoFe_2O_4 (Fig. 2a(i)) shows diffraction peaks characteristic only to CoFe_2O_4 ($2\theta = 30.1^\circ, 35.4^\circ, 37.1^\circ, 43.1^\circ, 53.4^\circ, 56.9^\circ$ and 62.6° ; Powder Diffraction File (PDF): 00-022-1086). However, the mixed materials, 80 wt% CoFe_2O_4 (Fig. 2a(ii)) and 50 wt% CoFe_2O_4 (Fig. 2a(iii)) show patterns of both CoFe_2O_4 and CeZrO_2 ($2\theta = 29.1^\circ, 33.7^\circ, 48.4^\circ$ and 57.5° ; PDF: 00-038-1439). For lower loading of CoFe_2O_4 , i.e. in 20 wt% CoFe_2O_4 (Fig. 2a(iv)), only diffraction peaks of CeZrO_2 are present.

Similarly, pure NiFe_2O_4 and Ni-ferrites modified with CeZrO_2 were characterized using XRD (Fig. 2b). In bulk NiFe_2O_4 , only peaks corresponding to NiFe_2O_4 ($30.3^\circ, 35.7^\circ, 37.3^\circ, 43.4^\circ, 53.8^\circ, 57.3^\circ$ and 62.9° ; PDF: 00-010-0325) are observed (Fig. 2b(i)). XRD peaks of both NiFe_2O_4 and CeZrO_2 are identified in 80 wt% NiFe_2O_4 (Fig. 2b(ii)) and 50 wt% NiFe_2O_4 (Fig. 2b(iii)). In 20 wt% NiFe_2O_4 , again only diffractions corresponding to CeZrO_2 are found (Fig. 2b(iv)).

The crystallite sizes of the different phases in these materials were calculated from XRD using the Scherrer equation [41] and are represented in Fig. 3a. Among the CoFe_2O_4 materials, the largest crystallite size is observed in bulk CoFe_2O_4 (~ 57 nm). Upon addition of CeZrO_2 , a smaller crystallite size of CoFe_2O_4 is found in 80 wt% CoFe_2O_4 (~ 25 nm) and 50 wt% CoFe_2O_4 (~ 22 nm). So, the crystallite size reduces to less than half upon addition of CeZrO_2 . The crystallite size of CoFe_2O_4 in 20 wt% CoFe_2O_4 could not be determined by XRD as no characteristic peaks were observed (Fig. 2a(iv)). The crystallite size of CeZrO_2 varies between ~ 7 and 9 nm among these materials with a slight increase in crystallite size with progressive loading of CeZrO_2 (Fig. 3a).

All error bars represent standard deviation with 68% confidence

interval. The error bars in crystallite size calculation from XRD originate from averaging the crystallite size of the 4 most intense peaks and the error bars in BET surface area measurements were calculated from 4 measurements.

Among the Ni-ferrites, the highest crystallite size is obtained for bulk NiFe_2O_4 (~ 43 nm), while smaller crystallite sizes appear in 80 wt % NiFe_2O_4 (~ 24 nm) and 50 wt% NiFe_2O_4 (~ 20 nm). The addition of CeZrO_2 leads to a decline of NiFe_2O_4 crystallite size by close to half in comparison to bulk NiFe_2O_4 . In 20 wt% NiFe_2O_4 , no diffraction peaks of NiFe_2O_4 were observed due to fine dispersion of the spinel crystallites. Like in the Co-ferrites modified with CeZrO_2 , the crystallite size of CeZrO_2 in these materials slightly increases from ~ 7 to 9 nm, with increasing loading of CeZrO_2 (Fig. 3a). The surface area measurements (Fig. 3b) show a larger surface area in ferrites modified with CeZrO_2 in comparison to bulk ferrites. A progressive increase in surface area is seen with increasing loading of CeZrO_2 in both the Co- and Ni- modified ferrites. The highest surface area is found for 20 wt% CoFe_2O_4 and 20 wt% NiFe_2O_4 . Overall, the surface area and crystallite size calculations are in agreement with one another.

3.1.2. STEM-EDX analysis

The particle size and morphology in lower loadings of CoFe_2O_4 and NiFe_2O_4 were examined using STEM-EDX analysis, as the information about these phases could not be obtained from XRD. The morphology of 20 wt% CoFe_2O_4 (Fig. 4a) shows finely dispersed particles with average particle size ~ 8 nm.

The elemental mapping (Fig. 4b) of this image shows that Co and Fe remain finely dispersed. The occurrence of Co and Fe together suggests the formation of a spinel phase CoFe_2O_4 , in line with the samples with lower CeZrO_2 loadings, however localized Co and Fe rich clusters are also observed. The EDX overlay of Ce and Zr (Fig. 4c) shows a uniform distribution throughout the sample with localized Ce rich clusters.

A similar morphology with average particle size ~ 8 nm was identified for as prepared 20 wt% NiFe_2O_4 (Fig. 4d). The EDX overlay image (Fig. 4e) presents Ni and Fe together indicating a possible formation of NiFe_2O_4 . A uniform elemental distribution of Ce and Zr is obtained throughout (Fig. 4f) with some Ce rich clusters. The various phases identified are in agreement with the results obtained in XRD, i.e. both spinel phases of CoFe_2O_4 and NiFe_2O_4 are finely dispersed in CeZrO_2 . An additional HR-TEM analysis was also performed on 80 wt% $\text{CoFe}_2\text{O}_4/\text{NiFe}_2\text{O}_4$ and the results show the formation of respective spinel ($\text{CoFe}_2\text{O}_4/\text{NiFe}_2\text{O}_4$) and CeZrO_2 phases (Supplementary information Fig. S2) which are in line with the information obtained from XRD.

3.1.3. Redox properties: H_2/CO_2

The ferrite materials modified with CeZrO_2 were investigated for changes in redox properties during two consecutive cycles of H_2 -TPR and CO_2 -TPO. The phase changes were monitored during in situ XRD

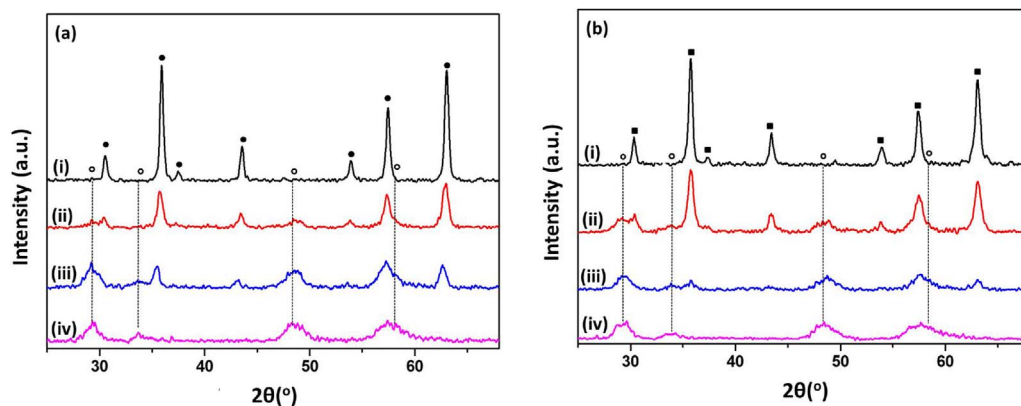
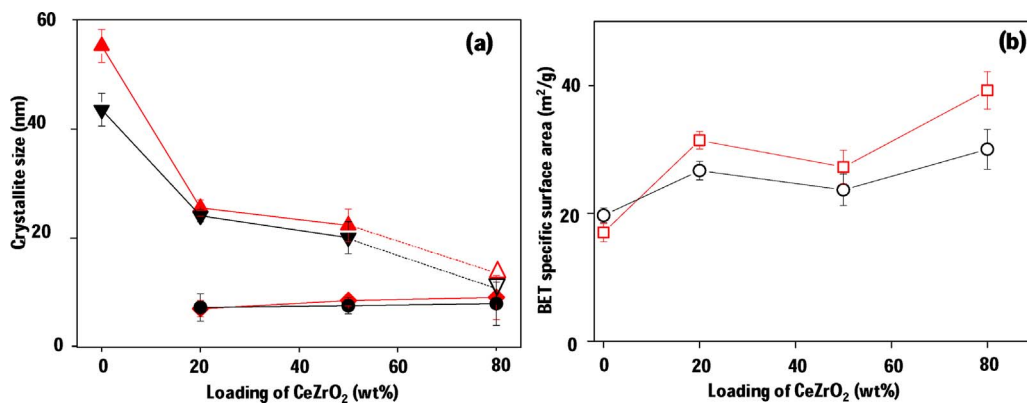


Fig. 2. The XRD patterns of as prepared (a) $\text{CoFe}_2\text{O}_4 - \text{CeZrO}_2$ and (b) $\text{NiFe}_2\text{O}_4 - \text{CeZrO}_2$ materials with varying loading: (i) 100 wt% $\text{NiFe}_2\text{O}_4/\text{CoFe}_2\text{O}_4$, (ii) 80 wt% $\text{CoFe}_2\text{O}_4/\text{NiFe}_2\text{O}_4$, (iii) 50 wt% $\text{CoFe}_2\text{O}_4/\text{NiFe}_2\text{O}_4$ and (iv) 20 wt% $\text{CoFe}_2\text{O}_4/\text{NiFe}_2\text{O}_4$. (●) CoFe_2O_4 , (■) NiFe_2O_4 , (○) CeZrO_2 .



experiments, while the overall temperatures of reduction and reoxidation were followed in conventional TPR-TPO experiments.

3.1.3.1. *CoFe₂O₄–CeZrO₂*. The in situ XRD study of 80wt%CoFe₂O₄ during the first cycle (Fig. 5a) shows diffraction patterns characteristic of CoFe₂O₄ ($2\theta = 35.4^\circ$ and 43.1°) and CeZrO₂ ($2\theta = 29.1^\circ$ and 33.7°). The spinel (CoFe₂O₄) reduces to an alloy of CoFe ($2\theta = 45.3^\circ$) at $\sim 480^\circ\text{C}$ with a short transition to FeO ($2\theta = 41.9^\circ$) before. However, no diffraction peaks corresponding to metallic Co ($2\theta = 44.3^\circ$) or Fe ($2\theta = 44.7^\circ$) appear during the H₂-TPR, indicating that these elements mainly reside in the CoFe alloy which remains stable up to $\sim 700^\circ\text{C}$.

In the subsequent CO₂-TPO (Fig. 5b), the alloy CoFe diffractions remain stable up to a temperature of $\sim 580^\circ\text{C}$ and then reoxidize back to CoFe₂O₄. No separate diffraction peaks of CoO ($2\theta = 34.1^\circ$, 39.6°) are identified, indicating that no phase segregation occurred. Similar phase transformations were observed during the second cycle of H₂-TPR and CO₂-TPO.

In the CeZrO₂ phase ($2\theta = 29.1^\circ$), no true transition due to phase transformation occurs as the in situ XRD intensity shows no visible variations during reduction (Fig. 5a) and reoxidation (Fig. 5b).

However, Ce⁴⁺ can partially reduce to Ce³⁺ in these temperature ranges [42,43]. On the other hand, ZrO₂ does not undergo reduction in the investigated temperature range, but is known to exhibit polymorphism, i.e. a structural transformation between cubic, tetragonal and monoclinic phases without any reduction of ZrO₂ at temperatures above 1000 °C [44–46]. The addition of ZrO₂ to cubic structures such as CeO₂ can however result in lower temperatures of reduction [32]. While bulk CeO₂ reduces at temperatures beyond 800 °C [42], a peak position analysis of the CeZrO₂ diffraction at $2\theta = 29.1^\circ$ (Fig. 5c) shows a shift towards a lower 2θ value around $\sim 400^\circ\text{C}$. This indicates partial reduction of CeZrO₂ occurs, owing to its redox couple (Ce⁴⁺/Ce³⁺), and at a much lower temperature than for pure CeO₂. During H₂-TPR, the replacement of Ce⁴⁺ with the larger cation Ce³⁺ induces a lattice parameter increase in its bulk fluorite lattice and, therefore, a lower 2θ position [24] (Fig. 5c). The reverse is observed during the reoxidation process at 500 °C (Fig. 5d). Hence, the peak position analysis shows partial reduction as well as reoxidation of CeZrO₂ at $\sim 400^\circ\text{C}$ and $\sim 500^\circ\text{C}$, respectively.

A redox study was also performed in a conventional TPR-TPO setup. The H₂-TPR shows a reduction peak maximum at $\sim 520^\circ\text{C}$ along with a

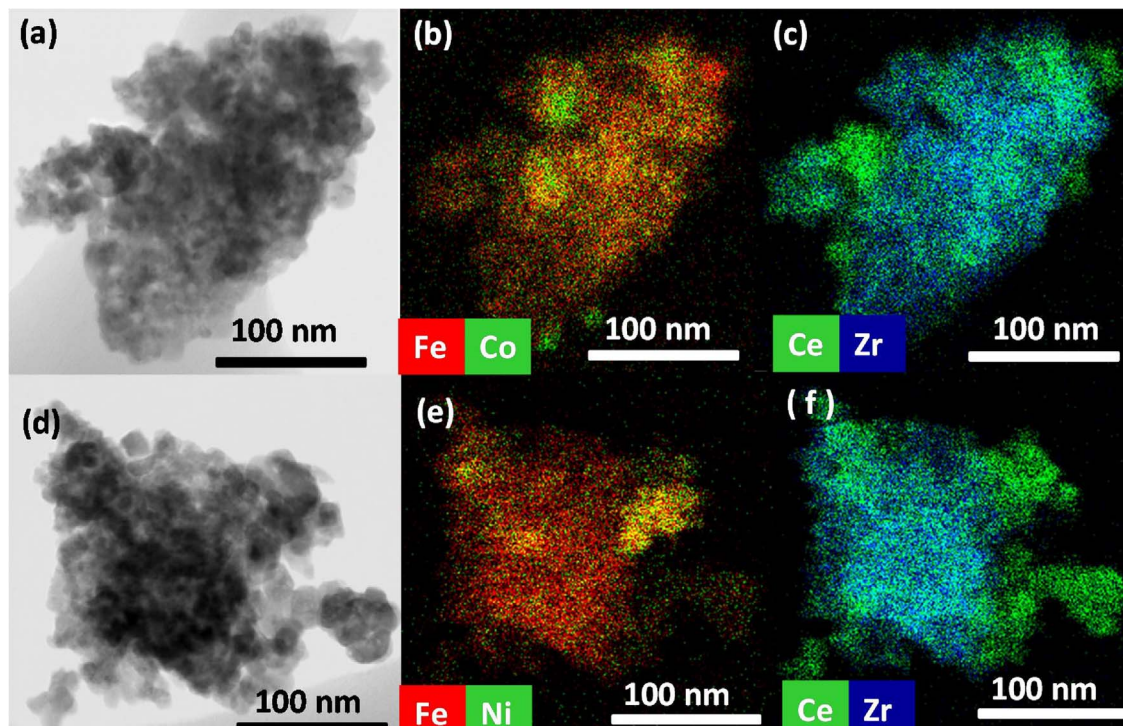


Fig. 4. STEM images of as prepared (a) 20 wt% CoFe₂O₄ showing the sample morphology and corresponding EDX elemental mapping of (b) Co and Fe along with (c) Ce and Zr. STEM micrographs of as prepared (d) 20 wt% NiFe₂O₄ showing the sample morphology and elemental mapping of (e) Ni and Fe along with (f) Ce and Zr.

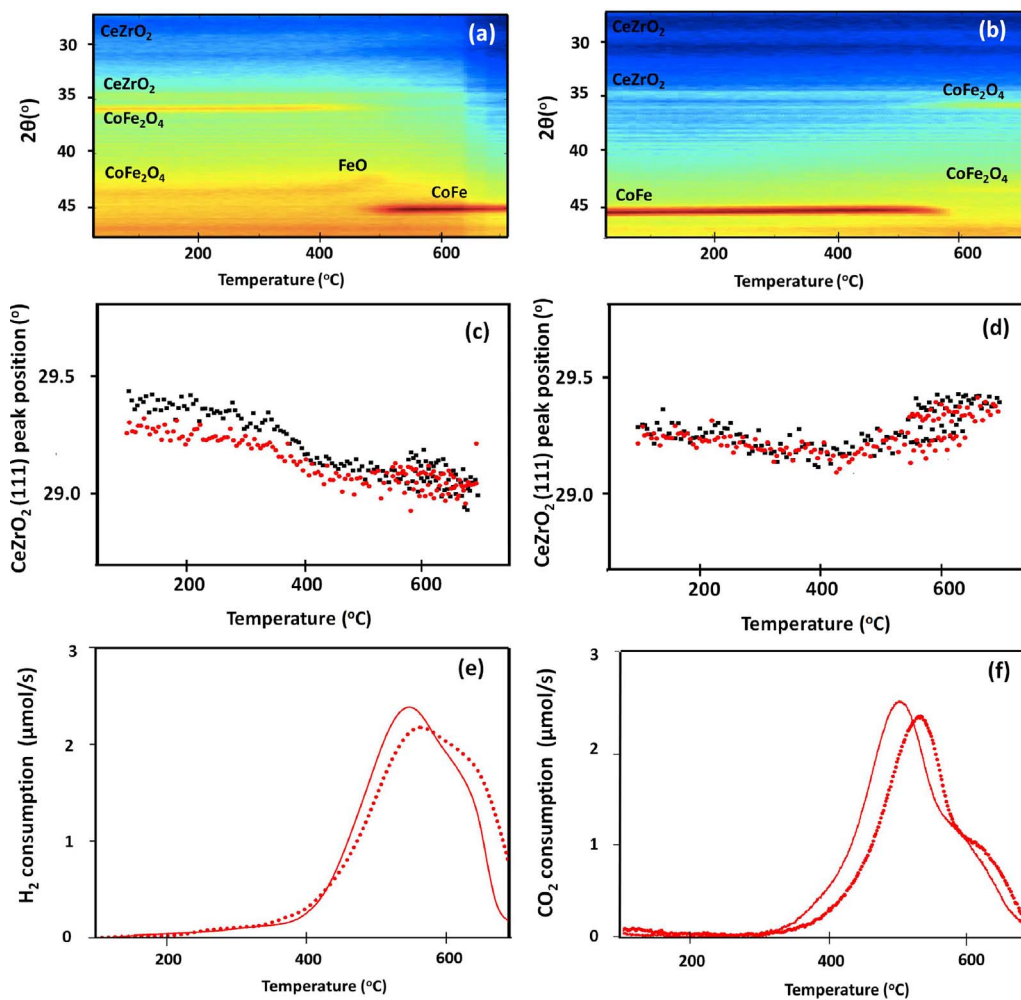


Fig. 5. H_2 -TPR and CO_2 -TPO of 80 wt% CoFe_2O_4 studied by in situ XRD and conventional TPR-TPO. The in situ XRD profiles showing phase transformations during the first cycle of (a) H_2 -TPR and (b) CO_2 -TPO along with the peak position changes in CeZrO_2 (111) during the two cycles of (c) H_2 -TPR and (d) CO_2 -TPO. The consumption profiles in conventional TPR-TPO during the two cycles of (e) H_2 -TPR and (f) CO_2 -TPO. CeZrO_2 (111) peak position during (●) first cycle and (■) second cycle. (—) First cycle and (.....) second cycle.

shoulder at ~ 620 °C (Fig. 5e). A similar profile is seen during the second cycle, with slightly higher temperatures of reduction with a peak maximum at ~ 550 °C and a shoulder at ~ 640 °C. The reduction shifts to higher temperature in comparison to the first cycle due to material sintering. During CO_2 reoxidation (Fig. 5f), the material shows two consumption peaks with a most intense peak at ~ 500 °C and a shoulder at ~ 600 °C. In the second cycle, the reoxidation shifts to a slightly higher temperature, with a maximum at ~ 550 °C and a small shoulder at ~ 630 °C. The conventional H_2 -TPR and CO_2 -TPO profiles were correlated with the crystallographic changes observed during the time resolved in situ XRD measurements. Thus, the onset of the reduction represents contributions from transformation of CoFe_2O_4 to FeO and CoFe alloy, along with the partial reduction of Ce^{4+} to Ce^{3+} in CeZrO_2 , as identified from in situ XRD. The peak maximum during the first and second cycle of H_2 -TPR mainly originates from the continued reduction of CoFe_2O_4 to CoFe alloy (see also supplementary information Fig. S3). The consumption shoulder at ~ 620 °C and ~ 640 °C during the first and second cycles of H_2 -TPR corresponds to the bulk reduction of the material. In the conventional CO_2 -TPO, the most intense peak during the two reoxidation cycles represents contributions from the partial reoxidation of Ce^{3+} to Ce^{4+} (Fig. 5d) and reoxidation of the alloy CoFe to spinel CoFe_2O_4 as seen from the peak position changes from the in situ XRD (Fig. 6).

The H_2 -TPR and CO_2 -TPO study show that the bulk of modified spinel material can repeatedly reduce (Fig. 5e) and reoxidize (Fig. 5f) at similar temperature (~ 550 °C) unlike the non-promoted CoFe_2O_4 (Supplementary information Fig. S4), in which reduction remains incomplete and the temperature of reduction shifts to much higher values

in the consecutive cycles during TPR due to material sintering. The non-promoted CoFe_2O_4 material shows reoxidation with CO_2 at ~ 580 °C during the two consecutive cycles, but during the second the amount of CO_2 consumption decreases as the reduction remains incomplete during the second H_2 -TPR. Moreover, the material suffered from sintering and phase segregation as evidenced from XRD (not shown). A similar redox analysis was performed on 50 wt% CoFe_2O_4 and 20 wt% CoFe_2O_4 (Supplementary information Fig. S5 & 6). In 50 wt% CoFe_2O_4 all the characteristic phases of CeZrO_2 and CoFe_2O_4 showed redox transitions similar to 80 wt% CoFe_2O_4 . However, in the lowest loading of CoFe_2O_4 i.e. in 20 wt% CoFe_2O_4 no separate diffraction peaks of spinel were identified but the presence of an alloy of CoFe phase during reduction and reoxidation showed that the finely dispersed spinel could reduce and reoxidize repeatedly. This redox analysis shows the spinel CoFe_2O_4 could equally reduce and reoxidize (~ 550 °C) to its as prepared state in all materials modified with CeZrO_2 .

3.1.3.2. NiFe_2O_4 – CeZrO_2 . The in situ XRD study of 80wt% NiFe_2O_4 during the first H_2 -TPR shows diffraction patterns of NiFe_2O_4 ($2\theta = 30.2^\circ$, 35.7° and 43.4°) and CeZrO_2 ($2\theta = 29.1^\circ$ and 33.7°). The spinel NiFe_2O_4 transforms to an alloy NiFe ($2\theta = 44.3^\circ$) and metallic Fe ($2\theta = 44.6^\circ$) at ~ 490 °C in the first cycle (Fig. 7a). At higher temperature, a fading diffraction peak of metallic Fe indicates that at ~ 650 °C most of the Fe is incorporated into the NiFe alloy. Unlike CoFe ferrites, the Ni -ferrites decompose to separate phases of Fe and an alloy of NiFe during the first H_2 -TPR cycle.

The in situ H_2 -TPR is followed by a CO_2 -TPO (Fig. 7b), during which the alloy segregates to metallic Ni ($2\theta = 44.5^\circ$) and Fe_3O_4 ($2\theta = 30.1^\circ$,

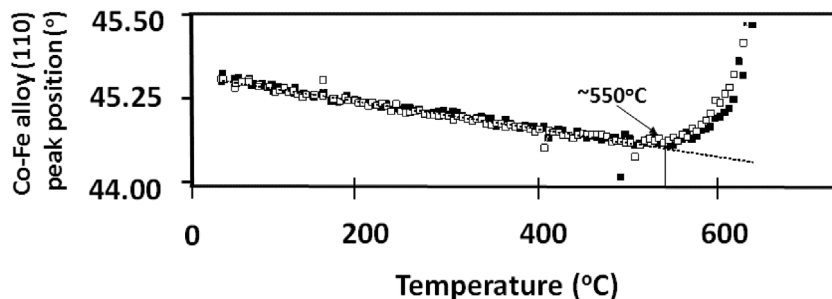


Fig. 6. Fitted peak position of alloy CoFe from the in situ XRD redox study of 80 wt% CoFe₂O₄ during the two CO₂-TPO cycles after H₂-TPR. (—) Trend line for thermal expansion in peak position during (□) first cycle and (■) second cycle.

35.5° and 43.1°; PDF: 03-065-3107) at ~550 °C. The presence of Fe₃O₄ can be discerned from the slightly lower 2θ values than for NiFe₂O₄. This suggests that Ni and Fe are present as metallic Ni and as Fe₃O₄ after reoxidation with CO₂, and hence the spinel NiFe₂O₄ phase no longer exists. No diffraction peaks of NiO (2θ = 43.3°) were identified during the H₂-TPR and CO₂-TPO. The material was again subjected to a second cycle of H₂-TPR, where Fe₃O₄ reduces to metallic Fe (~500 °C) and forms an alloy of NiFe with Ni (Fig. 7c). Unlike in the first H₂-TPR, where most of the Fe resides in the alloy NiFe, now it remains segregated as a separate Fe phase. When subjected to CO₂-TPO during the second cycle, segregated metallic Fe reoxidizes at ~450 °C, while the alloy NiFe again decomposes to metallic Ni and Fe₃O₄ at ~550 °C (Fig. 7d). No diffraction peaks of NiO were observed similar to the first H₂-TPR and CO₂-TPO. The CeZrO₂ peak position reveals no noticeable changes from the in situ XRD patterns, but the peak position analysis shows a partial reduction (~400 °C) and reoxidation (~500 °C) similar to the CeZrO₂ modified CoFe₂O₄ materials (not shown).

A conventional redox analysis was performed to identify the bulk reduction and reoxidation temperatures during the two redox cycles. During the first cycle of H₂-TPR, the material shows a consumption peak at ~490 °C and a shoulder around ~580 °C (Fig. 7e). However, during the second cycle of H₂-TPR, peaks shift to higher temperatures, with a first peak at ~530 °C and the second shoulder at ~600 °C. This first peak is due to the combined contribution from reduction of NiFe₂O₄ and partial reduction of CeZrO₂, similar to the CoFe₂O₄ modified ferrites. The presence of a shoulder at higher temperatures represents the bulk reduction of the material.

The CO₂-TPO profile during the first cycle (Fig. 7f) displays a broad peak at ~420 °C and a second peak with a maximum at ~600 °C. During the second cycle of reoxidation, temperatures shift to higher values with a shoulder at ~500 °C and the main consumption peak at ~610 °C. The presence of two reoxidation peaks during the consecutive cycles of CO₂-TPO indicate surface and bulk reoxidation.

Thus, from the TPR-TPO analysis it can be concluded that the 80 wt

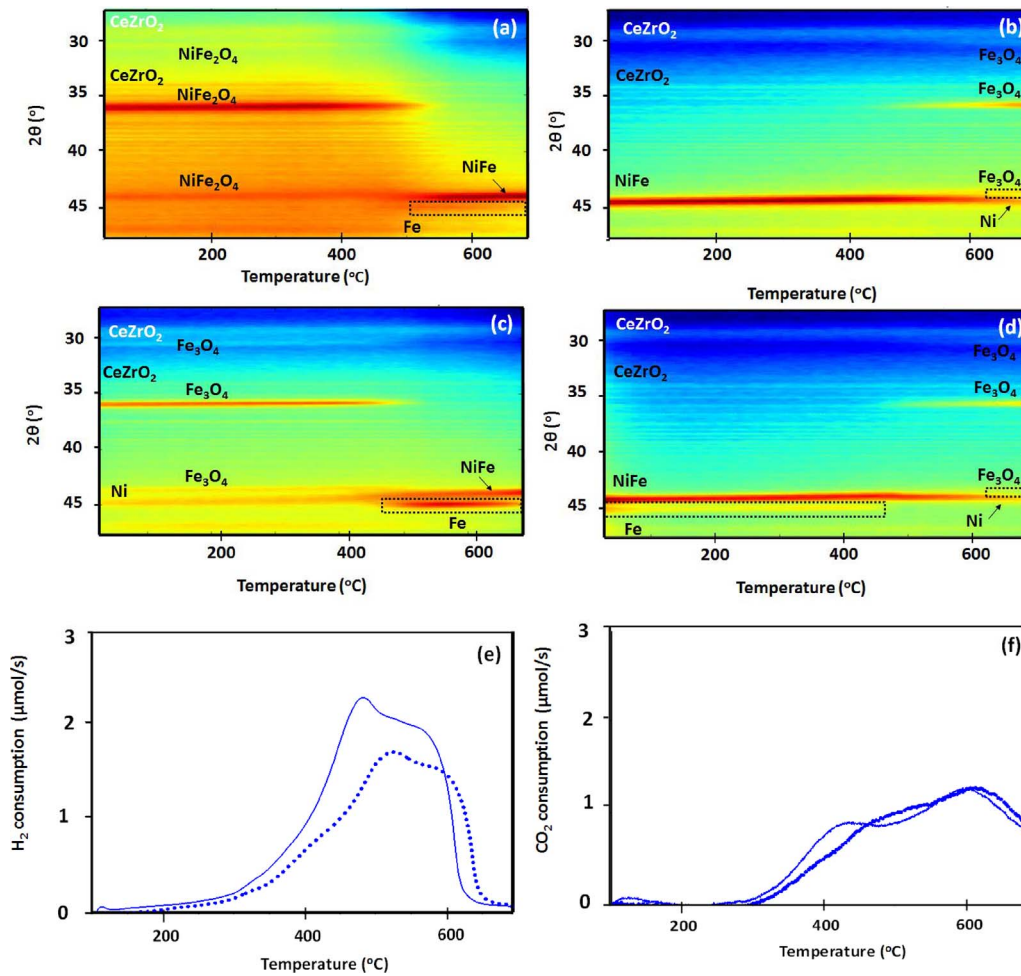
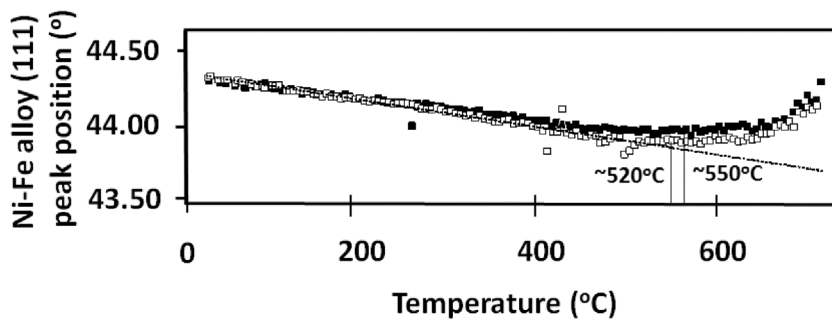


Fig. 7. H₂-TPR and CO₂-TPO of 80 wt% NiFe₂O₄ followed by in situ XRD and conventional TPR-TPO during two consecutive redox cycles. The in situ XRD profiles showing phase transformations during the first cycle with (a) H₂-TPR, (b) CO₂-TPO and second cycle of (c) H₂-TPR and (d) CO₂-TPO. The consumption profiles in a conventional TPR-TPO setup during the two cycles of (e) H₂-TPR and (f) CO₂-TPO. (—) First cycle and (.....) second cycle.



% NiFe₂O₄ material reduces to separate NiFe and Fe phases along with partial reduction of CeZrO₂. The NiFe alloy reoxidizes at 550 °C to Ni and Fe₃O₄ (Fig. 8), unlike bulk NiFe₂O₄ (Supplementary information Fig. S7). The latter material shows a relatively high temperature of reduction (~580 °C), and reoxidation profiles suggest not all the material could be reoxidized as indicated by the rising features beyond 600 °C. The reoxidation could be incomplete due to phase segregation during repeated redox cycling as indicated by XRD (not shown).

The redox analysis on the other loadings i.e. 50 wt% NiFe₂O₄ and 20 wt% NiFe₂O₄ (Supplementary information Fig. S8 & 9) showed that the reduction lead to separate NiFe and Fe phases and the spinel is not restored upon reoxidation. Hence, none of the CeZrO₂ modified Ni – ferrite materials could be repeatedly reduced and reoxidized as the ferrite phase is lost.

The modification of ferrites with CeZrO₂ thus has a beneficial effect on the redox properties in comparison to pure ferrites. The in situ XRD study shown that the addition of CeZrO₂ to Co-ferrites leads to repeatable redox transitions between a CoFe alloy and spinel (CoFe₂O₄), whereas in the case of CeZrO₂ modified Ni-ferrites the spinel (NiFe₂O₄) cycles between Fe and NiFe alloy, and Fe₃O₄ with Ni.

3.1.4. Thermodynamics

The thermodynamics of the redox behavior of bulk ferrites was studied using the EkvCalc software package. The equilibrium phase diagram of unmodified ferrites as a function of varying reduction ratios using different reducing (H₂, CO) and oxidizing (H₂O/CO₂) gases is illustrated in Fig. 9. In the case of CoFe₂O₄ (Fig. 9a), the spinel is stable at low reducing ratios (P_{CO}/P_{CO} + P_{CO₂} < 0.05) above a temperature of

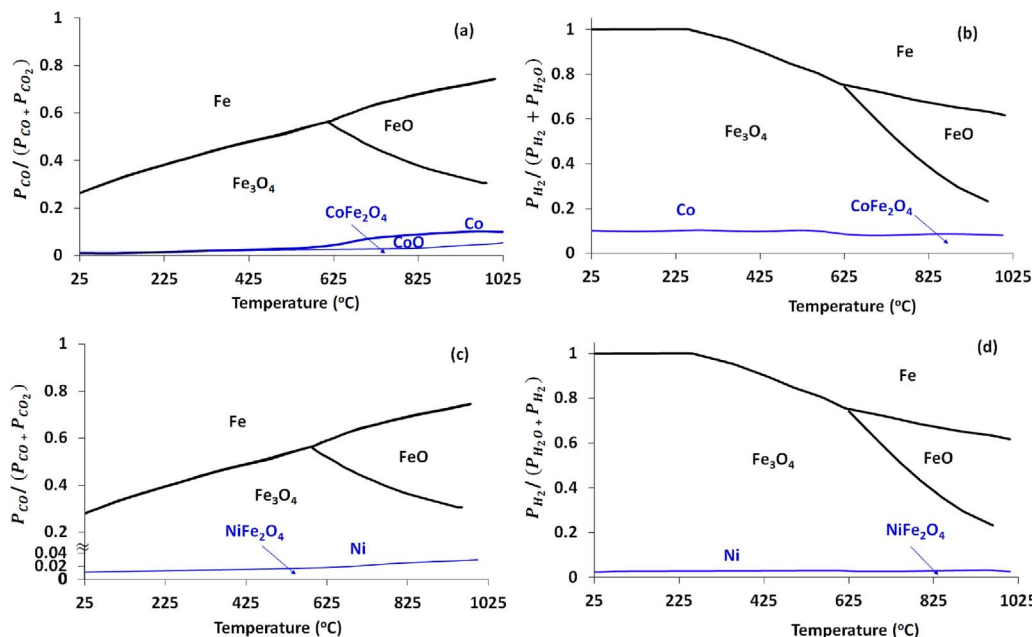


Fig. 8. Fitted peak position of alloy NiFe from the in situ XRD redox study of 80wt%NiFe₂O₄ during the two CO₂-TPO cycles after H₂-TPR. (—) Trend line for thermal expansion peak positions during (□) first cycle and (■) second cycle.

625 °C. At higher ratios (P_{CO}/P_{CO} + P_{CO₂} > 0.05) the spinel is decomposed into CoO and subsequently metallic Co, and Fe₃O₄ at P_{CO}/P_{CO} + P_{CO₂} > 0.1. At room temperature, Fe₃O₄ is the most oxidized form of iron oxide and a reduction to metallic Fe is only achieved at a reducing gas ratio (P_{CO}/P_{CO} + P_{CO₂}) > 0.26. However, with increasing temperature the region of direct reduction to Fe shifts to higher ratios. At a reducing ratio (P_{CO}/P_{CO} + P_{CO₂}) > 0.6 and in temperature ranges between 625 °C – 1025 °C, FeO appears as a transition of phase between Fe and Fe₃O₄. Deeper reduction to Fe is achieved only at high reducing ratios in these temperature ranges.

In a mixture of H₂/H₂O (Fig. 9b) the spinel is stable up to a reducing ratio of P_{H2}/P_{H2} + P_{H2O} < 0.1, which is slightly higher than the values observed with CO/CO₂ as reducing gas mixture. Above this ratio the spinel decomposes to metallic Co. Unlike with the CO/CO₂ redox mixture, no CoO phase was observed. At room temperature, Fe₃O₄ is the most oxidized form of Fe up to a temperature of ~275 °C. The formation of metallic Fe is observed at temperatures > ~275 °C and high reducing gas ratios (P_{H2}/P_{H2} + P_{H2O} ~ 1). In temperature ranges 625 °C – 1025 °C and at P_{H2}/P_{H2} + P_{H2O} > ~0.7, FeO is seen as a transition phase between Fe and Fe₃O₄. Deeper reduction to metallic Fe is observed at relatively higher reduction ratios in a mixture of H₂/H₂O in comparison to CO/CO₂.

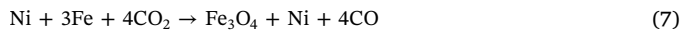
A similar analysis was performed on NiFe₂O₄ ferrites (Fig. 9c). The spinel NiFe₂O₄ is stable at low reduction ratio (P_{CO}/P_{CO} + P_{CO₂} < 0.02) and above this value the spinel is directly reduced to metallic Ni. Under the present conditions, formation of NiO is thermodynamically unfavorable. The occurrence of metallic Fe is seen at reducing ratios (P_{CO}/P_{CO} + P_{CO₂}) > 0.26 and below this ratio Fe₃O₄ is the most oxidized form

Fig. 9. The phase diagram of pure ferrite materials and respective metal oxides in the presence of different reducing and reoxidizing gases (CO + CO₂ and H₂ + H₂O). Equilibrium lines of pure (a) Co – ferrite and (c) Ni – ferrite materials with CO as reducing and CO₂ as reoxidizing gases. The equilibrium lines under H₂ and H₂O as reducing and reoxidizing gases respectively: (b) Co-ferrite and (d) Ni-ferrite. Blue lines: Co, resp. Ni related phases, black lines: Fe related phases. (For interpretation of the references to colour in this figure legend, the reader is referred to the web version of this article.)

of iron oxides. Again, with increasing temperature, Fe_3O_4 will only reduce to metallic Fe with a transition through FeO . This trend is seen above a reducing ratio ($P_{\text{CO}}/P_{\text{CO}} + P_{\text{CO}_2} > 0.6$) and in the temperature range 625 °C–1025 °C. The transition profiles of iron oxides in NiFe_2O_4 hence show a similar trend as for CoFe_2O_4 , but the region of thermodynamic stability is different for CoFe_2O_4 and NiFe_2O_4 .

When using $\text{H}_2/\text{H}_2\text{O}$ as a reducing mixture, the spinel NiFe_2O_4 (Fig. 9d) is stable at a relatively higher reduction ratio ($P_{\text{H}_2}/P_{\text{H}_2} + P_{\text{H}_2\text{O}} > 0.05$) in comparison to a CO/CO_2 reduction mixture. Any value higher than this ratio results in the formation of metallic Ni. The reduction to metallic Fe is seen at temperatures $> \sim 275$ °C and reducing ratios ($P_{\text{H}_2}/P_{\text{H}_2} + P_{\text{H}_2\text{O}} \sim 1$) and below this ratio Fe_3O_4 is the most oxidized form of iron oxides. Again, with increasing temperature, Fe_3O_4 reduces to metallic Fe with a transition through FeO above a reducing ratio ($P_{\text{CO}}/P_{\text{CO}} + P_{\text{CO}_2} > 0.7$) and in the temperature range 625 °C–1025 °C.

The *in situ* XRD study already gives an indication of the evolution of oxygen storage capacity upon cycling for the CeZrO_2 modified ferrites compared to pure ferrites and iron oxide as chemical looping material. From the Eq. (6), (7) below can be derived that, when pure Fe_3O_4 is used as oxygen carrier, for every mole of Fe consumed, 1.33 mol of CO is produced.



In the case of pure CoFe_2O_4 , 2 mol CO is produced per mole of Fe (Eq. (2)). This oxygen storage capacity remains enhanced as the reduced material always reoxidizes back to CoFe_2O_4 . For Ni-ferrites, the oxygen storage capacity is the same as for Fe_3O_4 (Eq. (6)) since the Ni-ferrite undergoes phase segregation to Fe_3O_4 and metallic Ni (Eq. (7)). The Co-ferrites modified with CeZrO_2 can reduce and reoxidize repeatedly at similar temperatures as shown from the *in situ* XRD redox study, in contrast to iron oxide, pure ferrites and modified Ni-ferrites.

3.1.5. Stability: H_2/CO_2

In addition to H_2 -TPR and CO_2 -TPO, isothermal cycling experiments were performed to study the stability and CO space time yield. The operating temperature was chosen based on the redox study described above in section 3.1.3.1 and 3.1.3.2. The bulk reoxidation of CoFe_2O_4 materials modified with CeZrO_2 occurred at ~ 550 °C as seen in the conventional TPR-TPO analysis (Fig. 5f). Moreover, from the CoFe alloy peak position analysis of the *in situ* XRD study, the alloy reoxidizes repeatedly at 550 °C (Fig. 6). Thus, a maximum utilization of oxygen storage capacity could be achieved by cycling between CoFe alloy and CoFe_2O_4 at this temperature.

For the Ni-ferrites modified with CeZrO_2 , a broad temperature window (~ 400 °C–600 °C) for reoxidation of the bulk materials was observed (Fig. 7f). The NiFe alloy (Fig. 8) reoxidized at ~ 550 °C through segregation into metallic Ni and Fe_3O_4 , but never reoxidized back to NiFe_2O_4 as confirmed by the *in situ* XRD analysis. Further increasing the temperature for redox cycling would only enhance the effect of sintering [20]. Therefore, the CO STY_M during prolonged isothermal cycling for both these ferrite materials was investigated at 550 °C over one hundred redox cycles (20 h time on stream, Fig. 10a & b).

Among the Co-ferrites modified with CoFe_2O_4 the highest CO STY_M is found for 20 wt% CoFe_2O_4 (Fig. 10a). Deactivation occurred up to ~ 20 redox cycles (4 h) and the STY_M remains stable thereafter. A similar trend was present in 50 wt% and 80 wt% CoFe_2O_4 at lower STY_M. In both materials a decline in activity was observed after the first ~ 10 cycles (2 h). The factors responsible for the decrease in STY_M were further examined using XRD of these materials after 100 isothermal cycles (Fig. 11a). In 20 wt% CoFe_2O_4 , unlike the as prepared sample (Fig. 11a(i)) where the spinel phase remained finely dispersed, a separate phase of CoFe_2O_4 (Fig. 11a(ii)) was discerned in the redox cycled

sample.

The prolonged cycling led to an increase of crystallite size due to sintering which allowed the detection of this phase (Fig. 11a(ii)). No diffraction peaks of metallic Co or Fe_3O_4 were identified, thus the spinel was not subject to phase segregation. The CeZrO_2 phase also suffered from sintering with a twofold increase in crystallite size (~ 20 nm). Hence, the deactivation in this material is attributed only to sintering.

In the higher loadings of CoFe_2O_4 (80 wt% CoFe_2O_4), the comparison between the as prepared (Fig. 11a(iii)) and prolonged cycled material (Fig. 11a(iv)) showed phase segregation. This suggests that the material could not be cycled back to the as prepared state. In addition to the CeZrO_2 peaks, separate phases of metallic Co, alloy CoFe and Fe_3O_4 (Fig. 11a(iv)) were identified. Large crystallites of Fe_3O_4 (~ 50 nm), metallic Co (~ 60 nm) and alloy CoFe (~ 50 nm) were formed upon cycling. Fe_3O_4 crystallites showed a twofold increase in crystallite size in comparison to the as prepared material. The formation of larger crystallites due to sintering could lead to an increased diffusion time in the bulk and result in incomplete oxidation leading to separate alloy CoFe and metallic Co phases even after reoxidation and resulting in phase segregation. Sintering of CeZrO_2 was less severe in comparison to higher loadings with an increase in crystallite size from ~ 7 nm in as prepared to ~ 12 nm in cycled materials. Hence, it is concluded that upon prolonged cycling, phase segregation of CoFe_2O_4 occurs, in addition to sintering of CeZrO_2 , both leading to deactivation. As a result, not all the CoFe_2O_4 in materials with lower CeZrO_2 loadings is cycled back to the as prepared state which results in a loss of oxygen storage capacity.

Among the Ni-ferrites modified with CeZrO_2 (Fig. 10b), 20 wt% NiFe_2O_4 shows the highest CO STY_M. Deactivation is observed during the first 20 cycles (4 h time on stream) and the STY_M remains stable thereafter. In the higher loadings of NiFe_2O_4 , both 50 wt% and 80 wt% NiFe_2O_4 show a decline in CO STY_M during the first 15 cycles and then remain stable till 100 cycles.

A detailed *ex situ* XRD analysis on 20 wt% NiFe_2O_4 material showed that unlike the as prepared material (Fig. 11b(i)), the redox cycled (Fig. 11b(ii)) showed separate peaks of metallic Ni appeared, indicating phase segregation even at lower ferrite loadings. A similar comparison was performed between as prepared (Fig. 11b(iii)) and redox cycled (Fig. 11b(iv)) 80 wt% NiFe_2O_4 . Phase segregation was also perceived in 80 wt% NiFe_2O_4 (Fig. 11b(iv)) with separate phases of metallic Ni and Fe_3O_4 . The CeZrO_2 suffered from heavy sintering, showing a twofold increase in crystallite size (~ 20 nm), similar to CeZrO_2 modified CoFe_2O_4 materials. In addition, large crystallite sizes of Fe_3O_4 (~ 75 nm) and metallic Ni (~ 50 nm) were found.

The crystallites of Fe_3O_4 exhibited a threefold increase in crystallite size in comparison to as prepared materials. Hence, for all the loadings of CeZrO_2 , both phase segregation and sintering lead to deactivation of CeZrO_2 – NiFe_2O_4 . Larger crystallites of Fe_3O_4 were observed in Ni-ferrites in comparison to Co-ferrites, indicate rapid sintering. The highest CO STY_M among both ferrites was exhibited by 20 wt% CoFe_2O_4 and 20 wt% NiFe_2O_4 . Among these, 20 wt% CoFe_2O_4 was the best performing material. The high redox activity is attributed to the repeatable reduction and reoxidation to the as prepared state. This is observed from both the *in situ* and *ex situ* XRD characterization, which shows repeated reoxidation to the spinel (CoFe_2O_4) state. The Ni-ferrites on the other hand suffered from phase segregation to Fe_3O_4 and metallic Ni, which led to reduced oxygen storage capacity and lower redox activity when compared to 20 wt% CoFe_2O_4 . Thus, 20 wt% CoFe_2O_4 was the best performing material and was examined further in chemical looping with alcohols.

4. Redox properties: alcohol/CO₂

Based upon the results of isothermal cycling (section 2.4), the stability of 20 wt% CoFe_2O_4 was investigated towards chemical looping with methanol and ethanol.

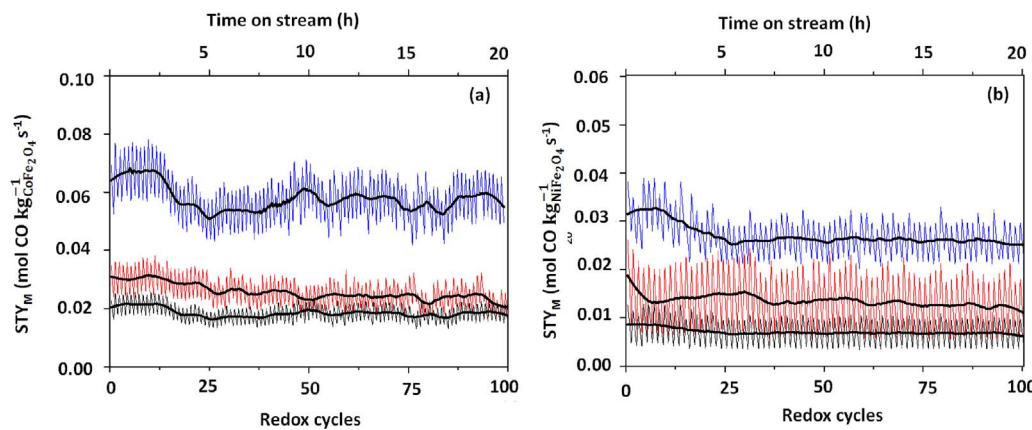
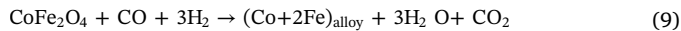


Fig. 10. The dynamic simulation of CO space time yield (STY_M) from the multi-tubular reactor configuration based on each of 100 isothermal redox cycles (20 h time on stream) in a single reactor experiment in (a) $CeZrO_2 - CoFe_2O_4$ and (b) $CeZrO_2 - NiFe_2O_4$ materials. The bold black line represents the time average of the STY_M (—) 20 wt % $CoFe_2O_4/NiFe_2O_4$, (—) 50 wt% $CoFe_2O_4/NiFe_2O_4$, (—) 80 wt% $CoFe_2O_4/NiFe_2O_4$.

4.1. Methanol

Chemical looping with methanol is carried out by pulsing methanol over the bifunctional material at 550 °C. Methanol undergoes decomposition (Eq. (8)) to produce CO and H_2 [47,48]. These products subsequently reduce the material resulting in the production of CO_2 and H_2O (Eq. 9).



The evolution of products during the reduction with methanol for 240 s (Fig. 12a) shows that the fuel is completely converted to CO_2 due to total oxidation during the reduction onset, later on CO and H_2 are the main products (Eq. (8)). The CO STY_M results on 20 wt% $CoFe_2O_4$ (Fig. 12b) showed that during the first four redox cycles (0.8 h) it exhibits a higher CO STY_M in comparison with H_2/CO_2 isothermal redox cycles (Fig. 10). A two to three times increase in CO STY_M was observed in both ferrites. A similar trend was observed in 20 wt% $NiFe_2O_4$ (Supplementary information Fig. S10), however it exhibited a CO STY_M lower than 20 wt% $CoFe_2O_4$.

Even with a reduction time of 60 s, a CO yield higher than the theoretical yield value was obtained as shown in Fig. 13a for 20 wt% $CoFe_2O_4$. This enhanced yield of CO can only be attributed to carbon formation during the reduction step and oxidation of carbon with CO_2 in the reoxidation step:



As the reduction time is increased to 180 and 300 s, the CO yield is multiplied by 2 and 3, respectively. For a reduction time of 480 s an almost 3.5 fold gain is seen. This study shows that in chemical looping with methanol, carbon formation is inevitable even when a cycle time as short as 60 s is employed (Fig. 13a). A similar trend in carbon

formation can be expected for Ni-ferrites as they also exhibit a CO STY_M higher than H_2/CO_2 redox cycles similar to Co-ferrites.

For complete gasification of carbon, air/O_2 is required [49]. Hence after each CO_2 reoxidation pulse, the material was oxidized with O_2 to quantify the total amount of carbon deposited. For a reduction half cycle of 60 s, the quantity of carbon oxidized with O_2 was three times higher than that of CO_2 (Fig. 13b). Further, for a reduction time of 180 s the oxidation of carbon with O_2 led to an increase of 1.5 times in comparison to reoxidation with CO_2 . When the reduction time was further prolonged to 300 and 480 s the carbon reoxidized was twice higher with O_2 than that of CO_2 .

The carbon formation was further investigated through a morphological and structural analysis by STEM on 20 wt% $CoFe_2O_4$ after chemical looping with methanol. Crystallites with varying diameter ($\sim 10-50$ nm) were observed (Fig. 14a). The EDX overlay of Co and Fe (Fig. 14b) shows that they occur together in larger crystallites, indicating the presence of the spinel i.e. $CoFe_2O_4$ phase. Some carbon appears in the neighborhood of the spinel phase. A similar STEM analysis was performed on 20 wt% $NiFe_2O_4$. The sample shows filaments (Fig. 14c) and large crystallites (~ 30 nm). Separate crystallites of Ni and Fe (Fig. 14d) are seen, indicating phase segregation. 20 wt% $CoFe_2O_4$ contained relatively large crystallites of Ni and carbon formation occurred, as observed in the Co-ferrite (Fig. 14b).

An additional ex situ XRD analysis was performed on both these materials after methanol chemical looping. The XRD comparison between as prepared (Fig. 15(i)) and redox cycled (Fig. 15(ii)) 20 wt% $CoFe_2O_4$ showed the formation of iron carbide (Fe_3C) and $CoFe_2O_4$. The presence of Fe_3C suggests carbon formation. The $CoFe_2O_4$ peaks after several chemical looping cycles with methanol show an increase in crystallite size due to sintering. This phenomenon was also observed for the $CeZrO_2$ phase which showed a 1.4 times increase in crystallite size (~ 13 nm). Thus, the STEM and XRD analysis show that deactivation of

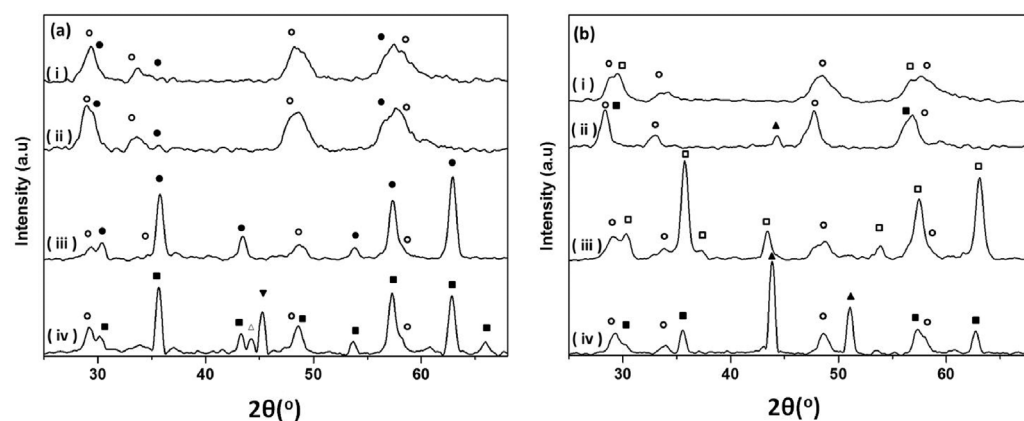
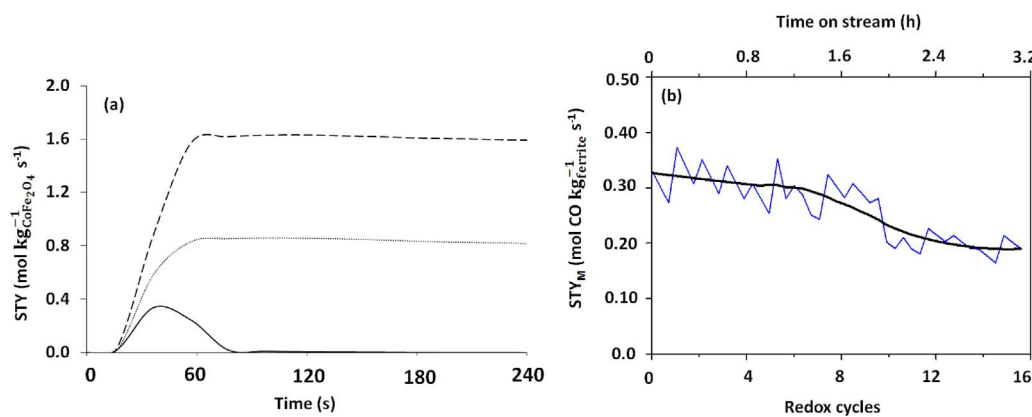


Fig. 11. XRD patterns of $CeZrO_2$ modified ferrites after 100 isothermal redox cycles (20 h time on stream) for (a) $CoFe_2O_4$ and (b) $NiFe_2O_4$. (i) as prepared and (ii) redox cycled 20 wt% $CoFe_2O_4/NiFe_2O_4$; (iii) as prepared and (iv) redox cycled 80 wt% $CoFe_2O_4/NiFe_2O_4$. (●) $CoFe_2O_4$, (▼) $CoFe$ alloy, (△) metallic Co, (■) Fe_3O_4 , (□) $NiFe_2O_4$ (▲) metallic Ni and (○) $CeZrO_2$.



20 wt% CoFe₂O₄ during cycling with methanol can be attributed mainly to material sintering.

The ex situ XRD study on as prepared (Fig. 15(iii)) and redox cycled (Fig. 15(iv)) on 20 wt% NiFe₂O₄ showed diffraction patterns of metallic Ni, Fe₃C and Fe₃O₄ resulting from phase segregation of NiFe₂O₄ after the reaction. The presence of Fe₃C follows from carbon formation. Further, sintering of the CeZrO₂ phase led to an increase of crystallite size by 1.7 times (~15 nm). Thus sintering and phase segregation both resulted in deactivation in this material.

The STEM and XRD study show that among both ferrites, CoFe₂O₄ could retain its spinel state whereas NiFe₂O₄ underwent phase segregation to Ni and Fe phases. Thus, the oxygen storage capacity of CoFe₂O₄ remains preserved during chemical looping with methanol. Carbon formation was observed in both samples, but this deposited carbon enhanced the CO yield when reoxidized with CO₂. The amount of carbon reoxidized depends on the reduction time (Fig. 13a). For a reduction time of 180 s, not all carbon can be reoxidized as shown by STEM (Fig. 14b & d). This carbon can result in the blockage of active sites, especially in Ni-ferrites, where carbon formation is more intense. Hence, although the reoxidation with CO₂ yields an elevated CO yield at first for both ferrites, deactivation will eventually occur due to accumulated carbon, as not all carbon can be gasified using CO₂ [49].

4.2. Ethanol

The bifunctional materials were applied towards catalyst-assisted chemical looping with ethanol (Eq. (11)). The materials were tested at 550 °C as the redox study showed repeated reduction and reoxidation at this temperature. The decomposition of ethanol resulted in CH₄, CO and H₂ as the main products.



However, the conversion of ethanol was limited to ~40% and in

addition CH₄ produced remained unconverted. In order to operate at higher conversions of ethanol and promote the subsequent reaction of CH₄, a more elevated temperature was applied. Ethanol decomposition was complete at 750 °C, but even at this temperature CH₄ remained unreacted, likely due to blockage of the active sites by carbon from CO via the Boudouard reaction. Another option to convert methane more efficiently is to add water to the feed for removal of carbon. As an investigation of this alternative, reactions were carried out at 750 °C using an ethanol-water mixture instead of pure ethanol as fuel to provide further insight in the reaction of CH₄. Water is a major component in bio-ethanol but an excess of water will have an adverse effect on the bifunctional material by reoxidation of the alloy (reverse of Eq. (9)), hence a reaction mixture of ethanol-water (1:1 mol ratio) was investigated assuming that steam reforming would allow the conversion of CH₄ (Eq. (12)).

The highest CO STY_M is shown by 20 wt% CoFe₂O₄ (Fig. 16a), two times higher than for 20 wt% NiFe₂O₄ (Supplementary information S11). Again, no conversion of methane was observed, possibly because the ratio of Ni:Fe was not optimal [50,51]. At the investigated conditions only CO and H₂ act as reducers. This is a similar trend as for methanol (section 4.1). A study on varying reduction time of the ethanol-water mixture was performed on the most active material, 20 wt% CoFe₂O₄, showing that the CO yield increases with prolonged reduction time (Fig. 16b). However, the maximum experimental CO yield remains below the theoretical limit. This could be due to the presence of water in the feed which slows down the reduction to Fe, thus limiting the production of CO during reoxidation.

For this reason, the CO yield from feeding an ethanol-water mixture over 20 wt% CoFe₂O₄ remains below expectation at the investigated reduction times. A detailed ex situ XRD study was performed on as prepared (Fig. 17(i)) and redox cycled 20 wt% CoFe₂O₄ (Fig. 17(ii)). The redox cycled material showed peaks corresponding to spinel CoFe₂O₄ (Fig. 17(ii)). This can be attributed to an increase of crystallite size during prolonged cycles. The XRD analysis also showed an increase of crystallites in CeZrO₂ (~15 nm). Further, absence of separate peaks

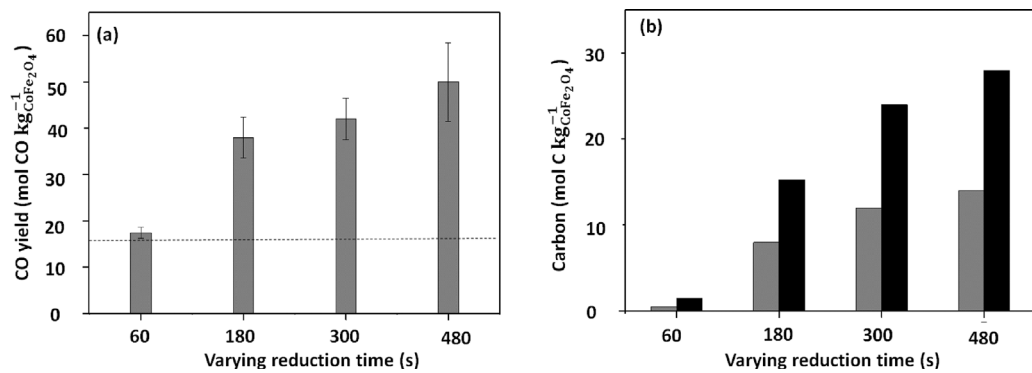


Fig. 13. Varying reduction time study showing the CO yield and carbon formation. (a) The CO yield in 20 wt% CoFe₂O₄ resulting from varying the reduction time with methanol. (—) Theoretical yield calculated from Eq. (2). (b) The carbon formation obtained after reoxidation with CO₂ and O₂ during the varying reduction time study. Bars with grey color represent (■) carbon from CO₂ reoxidation and black color (■) represent carbon from O₂ reoxidation.

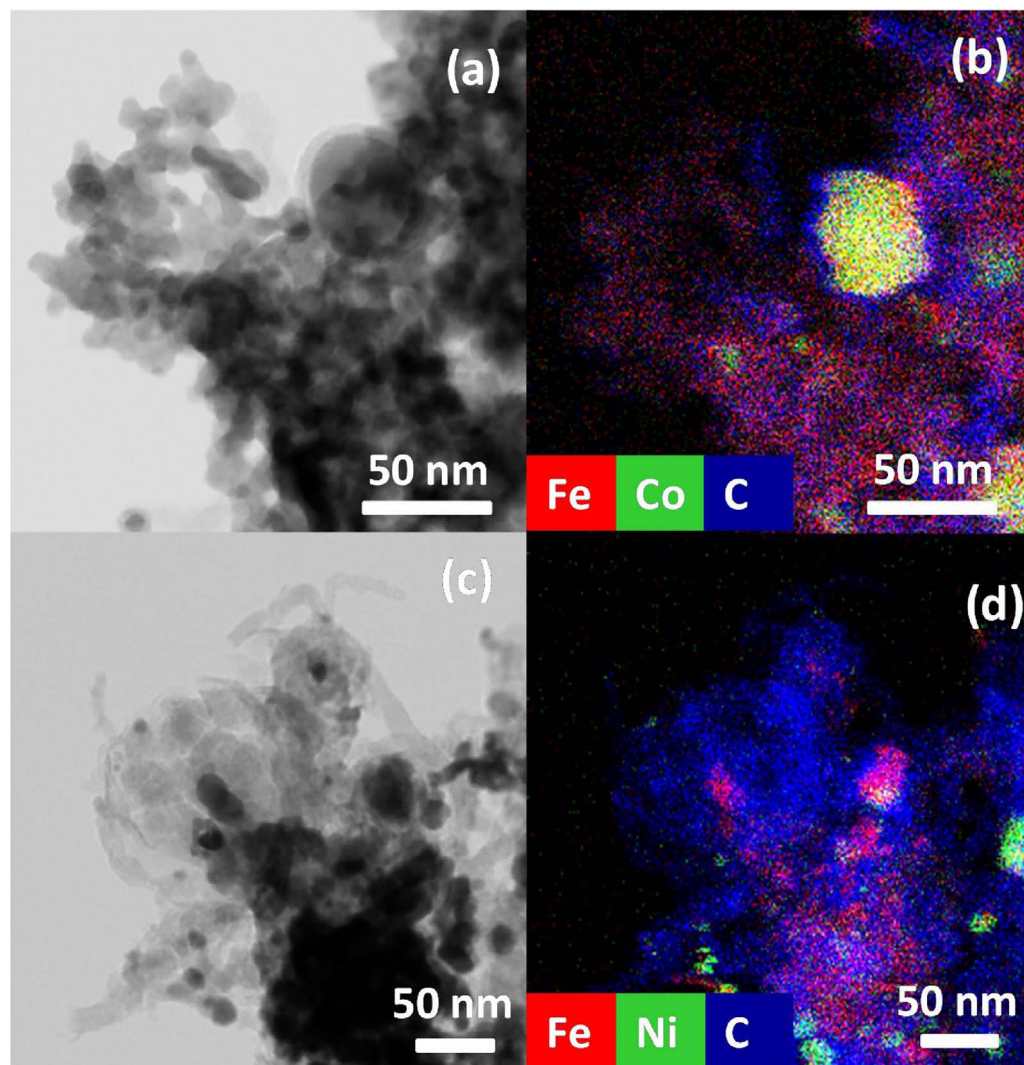


Fig. 14. STEM images of 20 wt% CoFe_2O_4 and 20 wt% NiFe_2O_4 after methanol redox cycles: (a) STEM micrograph and (b) EDX elemental mapping of Fe, Co and C in 20 wt % CoFe_2O_4 . (c) STEM image of 20 wt% NiFe_2O_4 and (d) EDX elemental mapping of Fe, Ni and C.

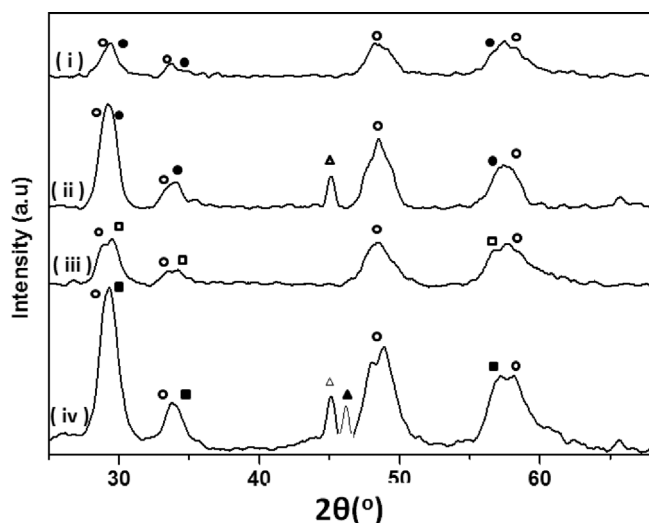


Fig. 15. XRD diffraction patterns after 15 chemical looping cycles (3 h time on stream) with methanol: (i) as prepared and (ii) redox cycled 20 wt% CoFe_2O_4 along with (iii) as prepared and (ii) redox cycled 20 wt% NiFe_2O_4 . Diffraction peak positions of (○) CeZrO_2 , (▲) metallic Ni, (△) Fe_3C , (□) NiFe_2O_4 , (●) CoFe_2O_4 and (■) Fe_3O_4 .

of metallic Co and Fe indicates no phase segregation occurred, thus deactivation can be attributed to material sintering.

A similar XRD study on as prepared (Fig. 17(iii)) and redox cycled 20 wt% NiFe_2O_4 (Fig. 17(iv)) showed phase segregation of spinel NiFe_2O_4 in this material. The redox cycled sample (Fig. 17(iv)) showed peaks of metallic Ni and Fe_3O_4 . The prolonged cycling led to an increased crystallite size of CeZrO_2 phase (~17 nm). Thus, both phase segregation and sintering lead to deactivation in this material.

The present results obtained with CeZrO_2 modified Co- and Ni-ferites are promising, but also indicate that there is room for improving these bifunctional materials. In particular, in chemical looping with ethanol, no conversion of methane was observed (Fig. 18a). A typical reduction half cycle with ethanol-water mixture (Fig. 18a) shows that CO_2 is initially the main product during the oxygen carrier reduction, after which CO , H_2 and CH_4 become increasingly dominant. Complete conversion of ethanol and CH_4 is not achieved during the reduction. At the investigated conditions only CO and H_2 act as reducers. The conversion of CH_4 can be achieved by a Ni based pre-catalyst bed [22,27].

Such configuration was tested using 10 wt% $\text{NiO}/\text{MgAl}_2\text{O}_4$ as pre-catalyst for chemical looping with the ethanol-water mixture. Initially, complete conversion of ethanol to CO_2 and H_2O was observed. With time, CO and H_2 were the main products and traces of CH_4 remained unconverted (Fig. 18b).

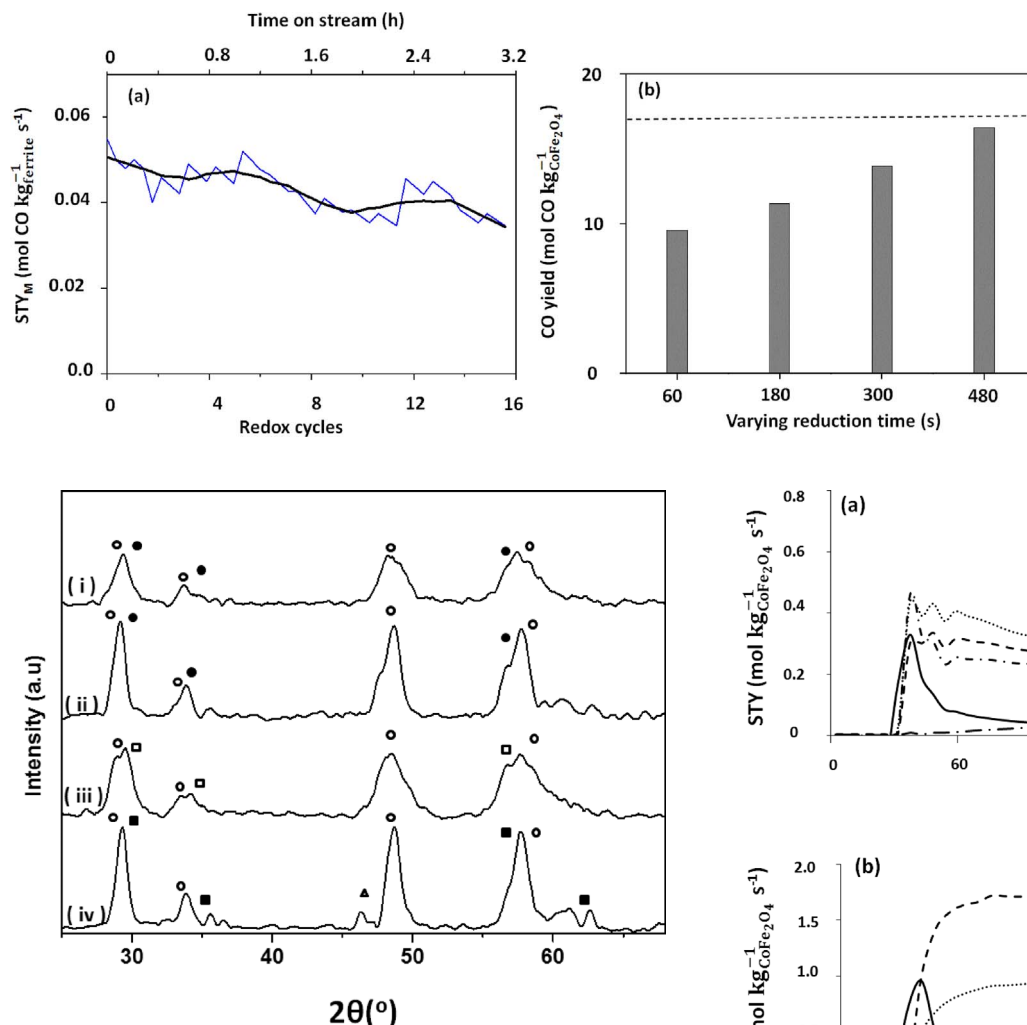


Fig. 17. XRD diffraction patterns after 15 chemical looping cycles (3 h time on stream) with ethanol: (i) as prepared and (ii) redox cycled 20 wt% CoFe_2O_4 ; (iii) as prepared and (ii) redox cycled 20 wt% NiFe_2O_4 . Diffraction peak position of (○) CeZrO_2 , (▲) metallic Ni, (□) NiFe_2O_4 , (●) CoFe_2O_4 and (■) Fe_3O_4 .

5. Conclusions

Co- and Ni-ferrites modified with CeZrO_2 were tested for their redox properties and applicability towards catalyst-assisted chemical looping processes with ethanol and methanol. The redox property investigations using in situ XRD along with conventional TPR-TPO showed that the Co-ferrites could reduce and reoxidize repeatedly between an alloy CoFe and CoFe_2O_4 phase. However, in Ni-ferrites, the material segregated into an alloy NiFe, metallic Ni, and Fe_3O_4 , which resulted in a loss of oxygen storage capacity in comparison to Co-ferrites. The highest CO production during isothermal cycles at 550 °C was shown by 20 wt% $\text{CoFe}_2\text{O}_4/\text{NiFe}_2\text{O}_4$.

In chemical looping with methanol, highest CO production was obtained in 20 wt% CoFe_2O_4 . The observed deactivation can be attributed to material sintering. The Co-ferrites could be reduced and reoxidized back to the as prepared state without loss in oxygen storage capacity. The Ni-ferrites suffered from sintering as well as phase segregation to metallic Ni and Fe_3O_4 resulting in a loss of oxygen storage capacity. Further, carbon formation led to an elevated CO yield upon reoxidation with CO_2 in both materials, even though it can lead to deactivation in the long run due to accumulation.

In chemical looping with ethanol, 20 wt% CoFe_2O_4 showed a threefold higher CO production than 20 wt% NiFe_2O_4 . Similar to

Fig. 16. (a) The dynamic simulation of CO Space time yield (STY_M) from the multi-tubular reactor configuration based on each of 15 chemical looping cycles (3 h time on stream) in as prepared 20 wt% CoFe_2O_4 with ethanol. The bold black line represents the time average of the STY_M . (—) 20 wt% CoFe_2O_4 (b) The CO yield for 20 wt% CoFe_2O_4 resulting from varying the reduction time. (—) Theoretical yield calculated from Eq. (2).

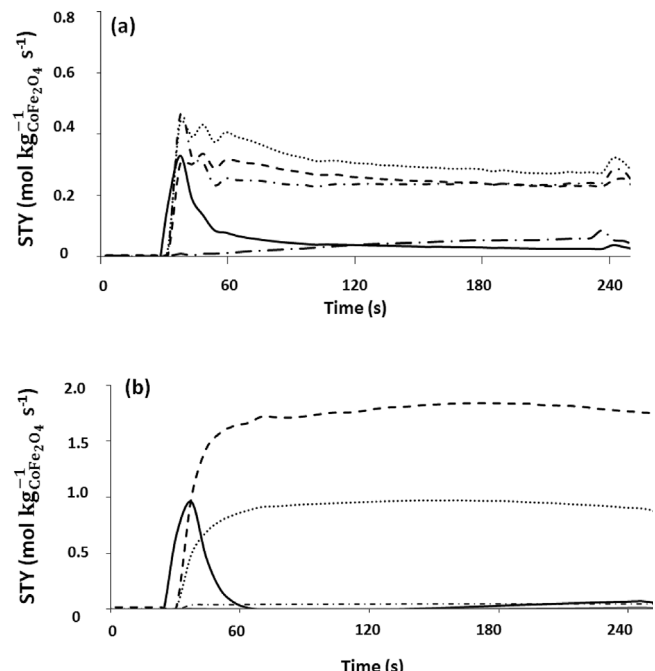


Fig. 18. Space time yield during the reduction step in chemical looping with ethanol-water mixture on 20 wt% CoFe_2O_4 , (a) without and (b) with pre-catalyst bed (—) CO_2 , (····) CO, (— · · · ·) CH_4 , (— · — ·) $\text{C}_2\text{H}_5\text{OH}$, (—) H_2 .

chemical looping with methanol, the Co-ferrites retained their oxygen storage capacity and did not suffer from phase segregation. In Ni-ferrites, the deactivation was a combination of sintering and phase segregation leading to a loss of oxygen storage capacity. Both materials were able to decompose ethanol to CO, H_2 and CH_4 , but could not convert CH_4 . In order to convert CH_4 , a pre-catalyst bed configuration is proposed.

Acknowledgements

This work was supported by the Long Term Structural Methusalem Funding by the Flemish Government, the Fund for Scientific Research Flanders (FWO; project G004613N), Promotion of Innovation through Science and Technology in Flanders (IWT Vlaanderen) and The Interuniversity Attraction Poles Programme, IAP7/5 Belgian State – Belgian Science Policy (BELSPO). The authors also thank Ir Laura Santander De Soto for her contribution and insights towards experimental analysis in the present study.

Appendix A. Supplementary data

Supplementary data associated with this article can be found, in the online version, at <http://dx.doi.org/10.1016/j.apcatb.2017.09.067>.

References

- [1] A. Levasseur, P. Lesage, M. Margni, L. Deschenes, R. Samson, *Environ. Sci. & Technol.* 44 (2010) 3169–3174.
- [2] E. Zedillo, *Global Warming Looking Beyond Kyoto*, (2008), pp. 1–10.
- [3] N.Z. Muradov, T.N. Veziroğlu, *Int. J. Hydrogen Energy* 33 (2008) 6804–6839.
- [4] A. Midilli, I. Dincer, M. Ay, *Energy Policy* 34 (2006) 3623–3633.
- [5] Y.J. Leng, S.H. Chan, S.P. Jiang, K.A. Khor, *Solid State Ionics* 170 (2004) 9–15.
- [6] K. Irshad, R. Siraj, F. Raza, M. Javed, I. Ahsan, M.S. Shakir, *AIP Adv.* 6 (2016).
- [7] C.D. Zuo, S.W. Zha, M.L. Liu, M. Hatano, M. Uchiyama, *Adv. Mater.* 18 (2006) 3318–3320.
- [8] A. Ideris, E. Croiset, M. Pritzker, *Int. J. Hydrogen Energy* (2017).
- [9] S. Sengodan, S. Choi, A. Jun, T.H. Shin, Y.-W. Ju, H.Y. Jeong, J. Shin, J.T.S. Irvine, G. Kim, *Nat. Mater.* 14 (2015) 205–209.
- [10] S. Park, J.M. Vohs, R.J. Gorte, *Nature* 404 (2000) 265–267.
- [11] V.M. Oetjen, U. Schmidt, F. Stimming, *J. Electrochem. Soc.* 143 (1996) 3838–3842.
- [12] G.H. Rau, *Energy Convers. Manage.* 45 (2004) 2143–2152.
- [13] D.H. Prasad, S.Y. Park, H. Ji, H.R. Kim, J.W. Son, B.K. Kim, H.W. Lee, J.H. Lee, *Appl. Catal. A* 411 (2012) 160–169.
- [14] W.Q. Shen, F.E. Huggins, N. Shah, G. Jacobs, Y.G. Wang, X.B. Shi, G.P. Huffman, *Appl. Catal. A* (2008) 102–110.
- [15] P.-C. Chiu, *Aerosol Air Qual. Res.* (2012).
- [16] A. Bayham, M. Tong, L.S. Kathe, *Wires. Energy. Environ.* 5 (2016) 216–241.
- [17] A. Nandy, C. Loha, S. Gu, P. Sarkar, M.K. Karmakar, P.K. Chatterjee, *Renew Sust Energ Rev.* 59 (2016) 597–619.
- [18] A. Abad, J. Adanez, F. Garcia-Labiano, L.F. de Diego, P. Gayan, J. Celaya, *Chem. Eng. Sci.* 62 (2007) 533–549.
- [19] J.P. Bohn, C.R. Cleeton, S.Y. Muller, S.A. Chuang, J.S. Scott, *Energy & Fuels* 24 (2010) 4025–4033.
- [20] V. Galvita, T. Hempel, H. Lorenz, L.K. Rihko-Struckmann, K. Sundmacher, *Ind. Eng. Chem. Res.* 47 (2008) 303–310.
- [21] M. Ismail, W. Liu, M.T. Dunstan, S.A. Scott, *Int. J. Hydrogen Energy* 41 (2016) 4073–4084.
- [22] L.C. Buelens, V.V. Galvita, H. Poelman, C. Detavernier, G.B. Marin, *Science* 354 (2016) 449–452.
- [23] V. Galvita, K. Sundmacher, *Appl. Catal. A* 289 (2005) 121–127.
- [24] V.V. Galvita, H. Poelman, C. Detavernier, G.B. Marin, *Appl. Catal. B* 164 (2015) 184–191.
- [25] L. Wang, D. Li, M. Koike, S. Koso, Y. Nakagawa, Y. Xu, K. Tomishige, *Appl. Catal. A* 392 (2011) 248–255.
- [26] V.V. Galvita, H. Poelman, E. Fornero, M. Saeys, G.B. Marin, *Development and Performance of Iron Based Oxygen Carriers for Chemical Looping, Nanotechnology in Catalysis*, Wiley-VCH Verlag GmbH & Co., 2017, pp. 421–448 (KGaA).
- [27] V.V. Galvita, H. Poelman, G.B. Marin, *Top. Catal.* 54 (2011) 907–913.
- [28] V.V. Galvita, H. Poelman, G.B. Marin, *J. Power Sources* 286 (2015) 362–370.
- [29] H.S. Lim, D. Kang, J.W. Lee, *Appl. Catal. B* 202 (2017) 175–183.
- [30] M. Cocchi, F. Mari, J.M.M. Cavani, *Appl. Catal. B* 152 (2014) 250–261.
- [31] C. Trevisanut, M. Mari, J.M.M. Millet, F. Cavani, *Int. J. Hydrogen Energy* 40 (2015) 5264–5271.
- [32] V. Galvita, L.K. Rihko-Struckmann, K. Sundmacher, *J. Mol. Catal. A Chem.* 283 (2008) 43–51.
- [33] A.J. Manukyan, A.V. Cross, S. Yeghishyan, J.J. Rouvimon, A.S. Miller, E.E. Mukasyan, *Appl. Catal. A* 508 (2015) 37–44.
- [34] A.L.A. Marinho, R.C. Rabelo-Neto, F.B. Noronha, L.V. Mattos, *Appl. Catal. A* 520 (2016) 53–64.
- [35] A. Tsioncheva, N. Gallo, M. Scotti, R. Dimitrov, E.M. Delaigle, D. Gaigneaux, V. Kovacheva, N. Dal Santo, *Appl. Catal. A* 417–418 (2012) 209–219.
- [36] H.B. Huang, L. Aisyah, P.J. Ashman, Y.C. Leung, C.W. Kwong, *Bioresour. Technol.* 140 (2013) 385–391.
- [37] C. Zhou, K. Shah, E. Doroodchi, B. Moghtaderi, *Energy Convers. Manage.* 96 (2015) 392–402.
- [38] H. Hong, Q.B. Liu, H.G. Jin, *J. Energy Resour. Technol. Asme* 131 (2009).
- [39] J. Hu, L. Buelens, S.-A. Theofanidis, V.V. Galvita, H. Poelman, G.B. Marin, *J. CO2 Util.* 16 (2016) 8–16.
- [40] B. Nolang, *Ekvincalc and Ekvibase; Version 4.30 Svensk Energi Data*, (2013) (Balinge, Sweden).
- [41] P. Scherrer, *Nachr. Ges. Wiss. Göttingen* 2 (1918) 98–100.
- [42] V.V. Galvita, H. Poelman, V. Bliznuk, C. Detavernier, G.B. Marin, *Ind. Eng. Chem. Res.* 52 (2013) 8416–8426.
- [43] N.V.R.A. Dharanipragada, M. Meledina, V.V. Galvita, H. Poelman, S. Turner, G. Van Tendeloo, C. Detavernier, G.B. Marin, *Ind. Eng. Chem. Res.* 55 (2016) 5911–5922.
- [44] P. Aldebert, J.P. Traverse, *J. Am. Ceram. Soc.* 68 (1985) 34–40.
- [45] J. Balducci, P. Kaspár, M. Fornasiero, M.S. Graziani, J.D. Islam, *J. Phys. Chem. B* 101 (1997) 1750–1753.
- [46] R.L. Oliveira, I.G. Bitencourt, F.B. Passos, *J. Braz. Chem. Soc.* 24 (2013) 68–75.
- [47] W.H. Cheng, *Acc. Chem. Res.* 32 (1999) 685–691.
- [48] H. Hong, T. Han, H.G. Jin, *J. Sol. Energ-T Asme* 132 (2010).
- [49] S.A. Theofanidis, R. Batchu, V.V. Galvita, H. Poelman, G.B. Marin, *Appl. Catal. B* 185 (2016) 42–55.
- [50] S.A. Theofanidis, V.V. Galvita, H. Poelman, G.B. Marin, *ACS Catal.* 5 (2015) 3028–3039.
- [51] S.A. Theofanidis, V.V. Galvita, M. Sabbe, H. Poelman, C. Detavernier, G.B. Marin, *Appl. Catal. B: Environ.* 209 (2017) 405–416.